

1 DLDTI: A learning-based framework for identification of drug-target interaction  
2 using neural networks and network representation

3 Yihan Zhao<sup>1‡</sup>, Kai Zheng<sup>2‡</sup>, Baoyi Guan<sup>3</sup>, Mengmeng Guo<sup>4</sup>, Lei Song<sup>1</sup>, Jie Gao<sup>3</sup>, Hua Qu<sup>3</sup>, Yuhui  
4 Wang<sup>4</sup>, Ying Zhang<sup>3\*</sup> and Dazhuo Shi<sup>3\*</sup>

5 <sup>1</sup> Department of Graduate School, Beijing University of Chinese Medicine, Beijing, China

6 <sup>2</sup> School of Computer Science and Engineering, Central South University, Changsha, China

7 <sup>3</sup> Cardiovascular Diseases Center, Xiyuan Hospital, China Academy of Chinese Medical Sciences,  
8 Beijing, China

9 <sup>4</sup> Institute of Cardiovascular Sciences, Health Science Center, Peking University, Key laboratory  
10 of Molecular Cardiovascular Sciences, Ministry of Education, Beijing, China

11 ‡ These authors contribute equally to this work.

12 \*Correspondence should be addressed to:

13 Ying Zhang and Dazhuo Shi, Cardiovascular Diseases Center, Xiyuan Hospital, China Academy  
14 of Chinese Medical Sciences, Beijing, China.

15 E-mail addresses: echo993272@sina.com (Y. Zhang) and shidztc@163.com (D.Z. Shi)

16

17

18 **Abstract**

19 To elucidate novel molecular mechanisms of known drugs, efficient and feasible  
20 computational methods for predicting potential drug-target interactions (DTI) would  
21 be of great importance. A novel calculation model called DLDTI was generated for  
22 predicting DTI based on network representation learning and convolutional neural  
23 networks. The proposed approach simultaneously fuses the topology of complex  
24 networks and diverse information from heterogeneous data sources and copes with the  
25 noisy, incomplete, and high-dimensional nature of large-scale biological data by  
26 learning low-dimensional and rich depth features of drugs and proteins.  
27 Low-dimensional feature vectors were used to train DLDTI to obtain optimal  
28 mapping space and infer new DTIs by ranking DTI candidates based on their  
29 proximity to optimal mapping space. DLDTI achieves promising performance under  
30 5-fold cross-validation with AUC values of 0.9172, which was higher than that of the  
31 method based on different classifiers or different feature combination technique.  
32 Moreover, biomedical experiments were also completed to validate DLDTI's  
33 performance. Consistent with the predicted result, tetramethylpyrazine, a member of  
34 pyrazines, reduced atherosclerosis progression and inhibited signal transduction in  
35 platelets, via PI3K/Akt, cAMP and calcium signaling pathways. The source code and  
36 datasets explored in this work are available at  
37 <https://github.com/CUMTzackGit/DLDTI>

38 **Keywords:** drug-target interaction; heterogeneous information; network  
39 representation learning; stacked auto-encoder; deep convolutional neural networks;  
40 atherosclerosis; signal transduction; tetramethylpyrazine

## 41 **Introduction**

42 Research on drug development is becoming increasingly expensive, while the number  
43 of newly approved drugs per year remains quite low [1][2]. In contrast to the classical  
44 hypothesis of “one gene, one drug, one disease”, drug repositioning aims to identify  
45 new characteristics of existing drugs [3]. Considering the available data on safety of  
46 already-licensed drugs, this approach could be advantageous compared with  
47 traditional drug discovery, which involves extensive preclinical and clinical studies  
48 [4]. Currently, a number of existing drugs have been successfully tuned to the new  
49 requirements. Methotrexate, an original cancer therapy, has been used for the  
50 treatment of rheumatoid arthritis and psoriasis for decades [5]. Galanthamine, an  
51 acetylcholinesterase inhibitor for treating paralysis, has been approved for  
52 Alzheimer’s disease [6].

53 Besides the evidence based on biological experiments and clinical trials,  
54 computational methods could facilitate high-throughput identification of novel target  
55 proteins of known drugs. To discover targets of drugs with known chemical structures,  
56 the prediction of drug-target interaction (DTI) based on numerous computational  
57 approaches have provided an alternative to costly and time-consuming experimental  
58 approaches [7]. In the past years, DTI prediction has bolstered the identification of  
59 putative new targets of existing drugs [8]. For instance, the computational pipeline  
60 predicted that telmisartan, an angiotensin II receptor antagonist, had the potential of  
61 inhibiting cyclooxygenase. In vitro experimental evidence also validated the  
62 predicted targets of this known drug [9]. Further, combined with in silico prediction,  
63 in vitro validation and animal phenotype model demonstrated that, topotecan, a  
64 topoisomerase inhibitor also had the potential to act as a direct inhibitor of human  
65 retinoic-acid-receptor-related orphan receptor-gamma t (ROR- $\gamma$ t) [10].

66 Most existing prediction methods mainly extract information from complex networks.  
67 Bleakley et al. [11] proposed a support vector machine-based method for identifying  
68 drug-target interactions based on bipartite local model (BLM). Mei et al. [12]  
69 proposed BLMNII method for predicting DTIs based on the bipartite local model and

70 neighbor-based interaction-profile inference. In addition, some researchers adopted  
71 kernelized Bayesian matrix factorization to predict DTIs, called KBMF2K [13]. A key  
72 step of KBMF2K is utilizing dimensional reduction, matrix factorization, and binary  
73 classification. Although homogenous network-based derivation methods have  
74 achieved good results, they are less effective in low-connectivity (degree) drugs for  
75 known target networks. The introduction of heterogeneous information can provide  
76 more perspective for predicting the potential of DTI. Recently, Luo et al. proposed a  
77 heterogeneous network-based unsupervised method for computing the interaction  
78 score between drugs and targets, called DTInet [9]. Subsequently, they proposed a  
79 neural network-based method [14] for improving the prediction performance of DTI.  
80 Effective integration of large-scale heterogeneous data sources is crucial in academia  
81 and industry.

82 Tetramethylpyrazine (TMPZ) is a member of pyrazines derived from Rhizoma  
83 Chuanxiong Hort [15]. According to a recent review, TMPZ could attenuate  
84 atherosclerosis by suppressing lipid accumulation in macrophages [16], alleviation of  
85 lipid metabolism disorder [17], and attenuation of oxidative stress [18]. However,  
86 since atherosclerosis is a chronic illness involving multiple cells and cytokines [19],  
87 besides lipoprotein metabolism and oxidative stress, other possible targets of TMPZ  
88 on atherosclerosis remain unexplored.

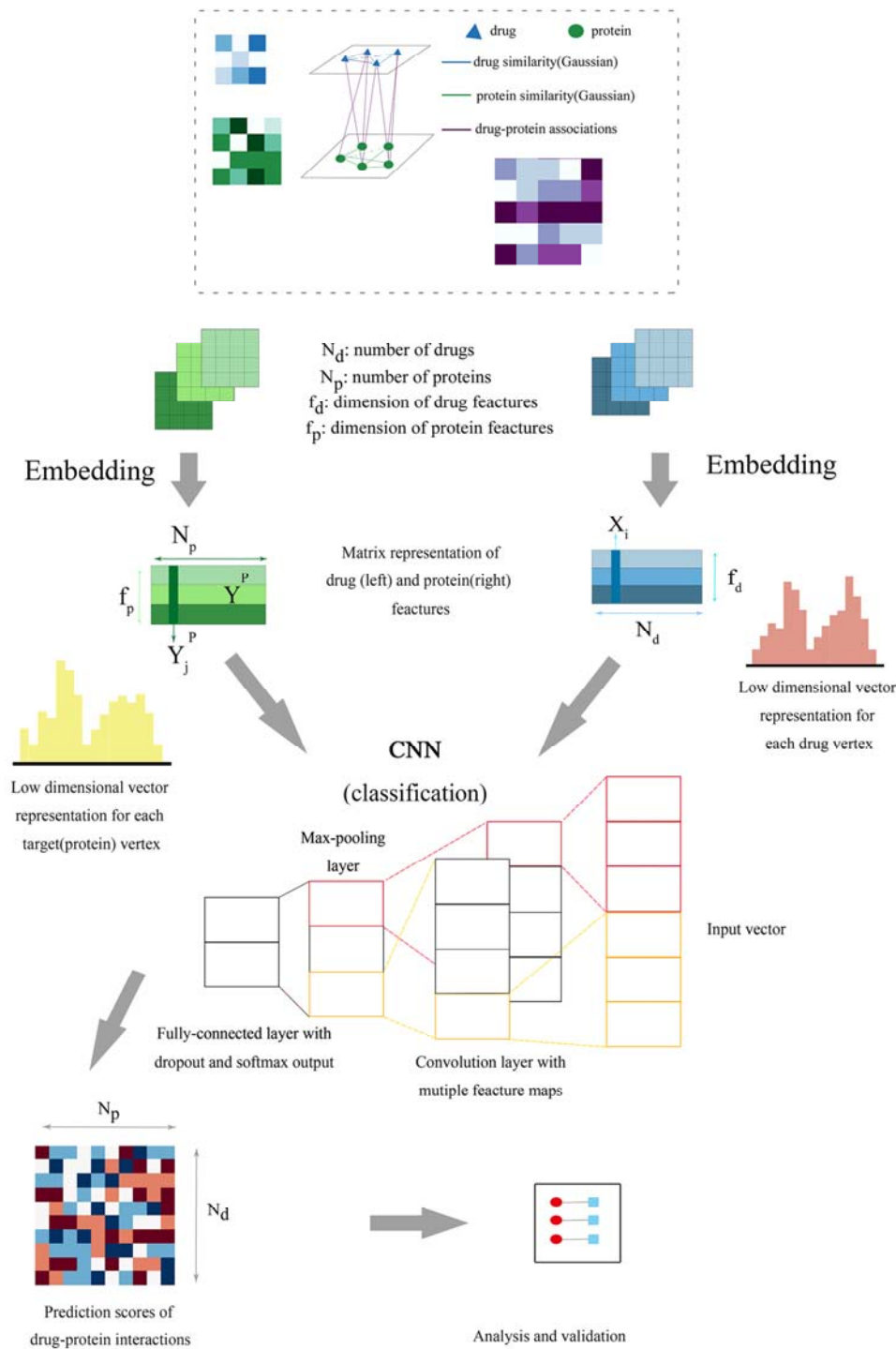
89 In this study, a novel model for prediction of DTI based on network representation  
90 learning and convolutional neural networks, referred to as DLDTI is presented for in  
91 silico identification of target proteins of known drugs. New DTIs were inferred by  
92 integrating drug- and protein-related multiple networks, to demonstrate the DLDTI's  
93 ability of integrating heterogeneous information and neural networks to extract deep  
94 features of drugs and target networks as well as attributes to effectively improve  
95 prediction accuracy. Moreover, comprehensive testing demonstrated that DLDTI  
96 could achieve substantial improvements in performance over other prediction  
97 methods. Based on the results predicted by DLDTI, new interactions between TMPZ  
98 and targets involved in atherosclerosis, namely signal transduction in platelets, were

99 validated in vivo. The anti-atherosclerosis effect of TMPZ was confirmed in a novel  
100 atherosclerosis model. In summary, these improvements could advance studies on  
101 drug-target interaction.

## 102 **Results**

### 103 **Overview of DLDTI and performance evaluation on predicting drug-target** 104 **interaction**

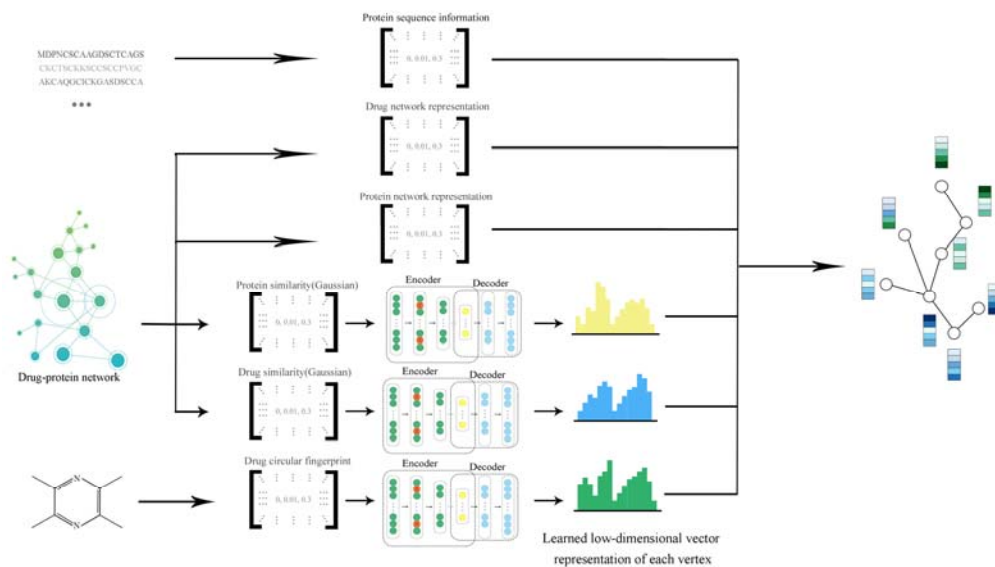
105 A new computational model referred to as DLDTI was developed to predict potential  
106 DTIs to identify novel behavior of traditional drugs based on complex networks and  
107 heterogeneous information. As an overview (Figure 1), DLDTI integrates learning  
108 from complex network's various heterogeneous information to obtain  
109 low-dimensional and deep rich features (Figure 2), through a processing method  
110 known as compact feature learning. During compact feature learning, the resulting  
111 low-dimensional descriptor integrates attribute characteristics, interaction information,  
112 relational properties, and network topology of each protein or target node in the  
113 complex network. DLDTI then determines the optimal mapping from the plenary  
114 mapping space to the prediction subspace, and whether the feature vector is close to  
115 the known correlations. Afterwards, DLDTI infers the new DTIs by ranking the  
116 drug-target interaction candidates according to their proximity to the predicted  
117 subspace.



118

119 Figure 1. The flowchart of the DLDTI pipeline. DLDTI first integrates a variety of  
 120 drug-related information sources to construct a heterogeneous network and applies a  
 121 compact feature learning algorithm to obtain a low-dimensional vector representation  
 122 of the features describing the topological properties for each node. Next, DLDTI

123 determines the optimal mapping from the plenary mapping space to the prediction  
124 subspace, and whether the feature vector is close to the known correlations.  
125 Afterwards, DLDTI infers the new DTIs by ranking the drug-target interaction  
126 candidates according to their proximity to the predicted subspace

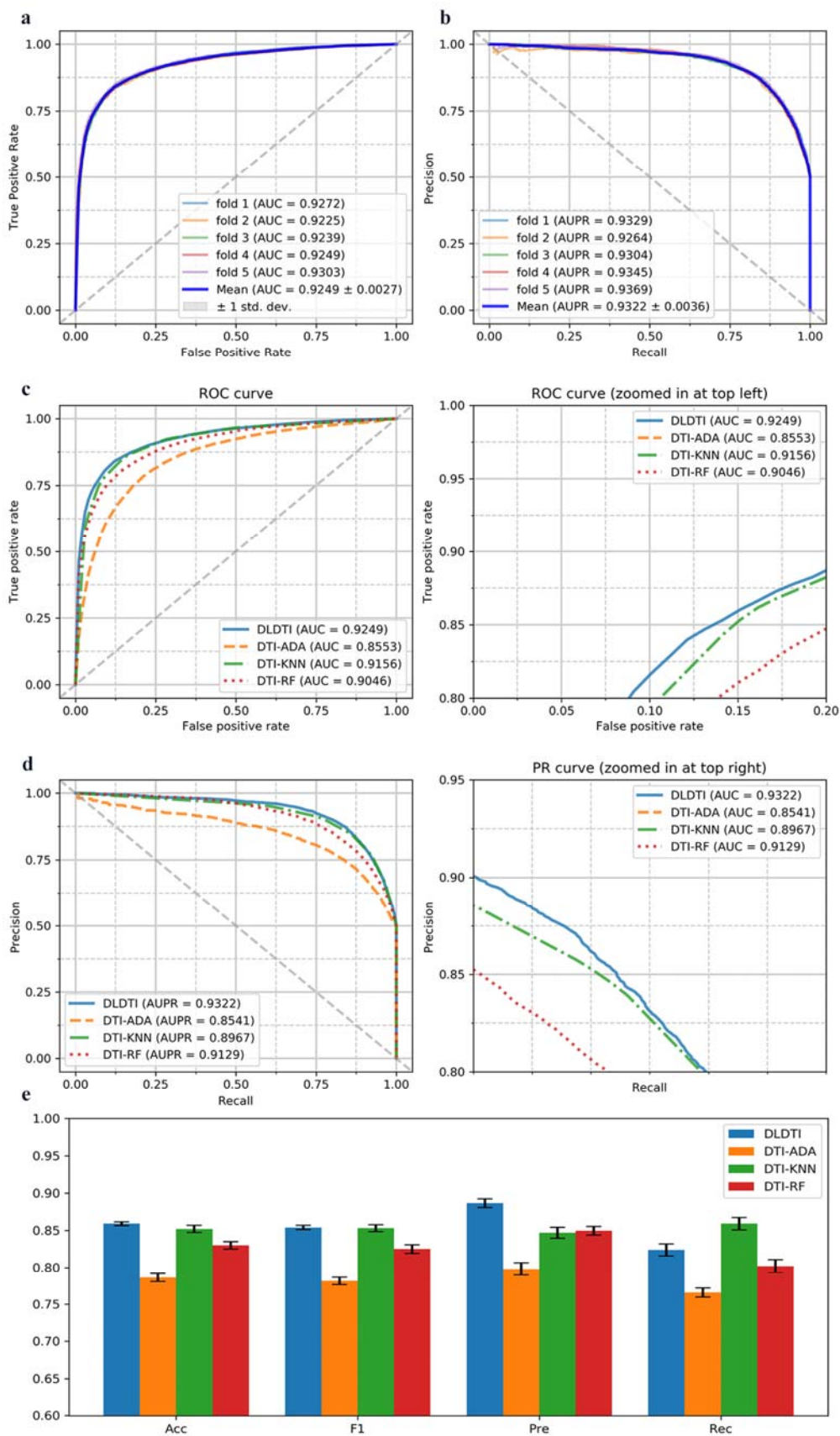


127  
128 Figure 2. Schematic illustration of compact feature learning. The Node2Vec  
129 algorithm is firstly used to calculate the topology information in complex networks.  
130 Gaussian interaction profile kernel similarity (GIP) and drug structure information are  
131 then extracted by a stacked automatic encoder, and the heterogeneous information is  
132 integrated to obtain a low-dimensional representation of the feature vector of each  
133 node. The resulting low-dimensional descriptor integrates the attribute characteristics,  
134 interaction information, relationship attributes and network topology of each protein  
135 or target node in the complex network.

136 DLDTI yields accurate DTI prediction. Firstly, the predictive performance of DLDTI  
137 was assessed using five-fold cross-validation, where randomly selected subset of  
138 one-fifth of the validated drug-target interaction were paired with an equal number of  
139 randomly sampled non-interacting pairs to derive the test set. The remaining 75% of  
140 known drug-target interaction and same number of randomly sampled non-interacting  
141 pairs were used to train the model. DLDTI was compared with three methods based  
142 on different classifiers used for DTI prediction, including DTI-ADA, DTI-KNN, and

143 DTI-RF [20][21][22]. The comparison revealed that DLDTI consistently outperforms  
144 the other three methods, with 0.93% higher AUC, 3.55% higher AUPR, 0.61% higher  
145 accuracy (Acc), 3.96% higher precision (Pre) than the second-best method (Fig. 3c,  
146 Fig. 3d and Fig. 3e). Compared to DTI-ADA (which predicts DTI based on the  
147 AdaBoost classifier), the DLDTI of the AUROC and AUPR was 6.96% and 7.81%  
148 higher, respectively, which could have been due to the inability of traditional machine  
149 learning to extract deeper abstract features for prediction, resulting in poor  
150 performance, while DLDTI applies a deep convolutional neural network approach and  
151 is able to capture the potential structural properties of complex networks and  
152 heterogeneous information.





154 Figure 3. Performance of DLDTI. (a) ROC curves performed by DLDTI model on  
155 DrugBank dataset. (b) PR curves performed by DLDTI model on DrugBank dataset.  
156 (c) Performance comparison (AUC scores) among four different prediction model  
157 which are DTI-ADA, DTI-KNN, and DTI-RF.(d)Performance comparison (AUPR  
158 scores) among four different prediction models including DTI-ADA, DTI-KNN, and  
159 DTI-RF.(e)Performance comparison (Acc., F1, Pre., Rec. scores) among DTI-ADA,  
160 DTI-KNN, and DTI-RF prediction models.

161 **Enrichment analysis suggested that TMPZ might affect signal transduction**  
162 **pathways involved in platelet activation**

163 To elucidate the potential function of TMPZ on atherosclerosis, the predicted results  
164 from DLDTI model were uploaded to the search tool for retrieval of interacting  
165 genes/proteins database (STRING, Version 11) (<https://string-db.org/>) [23] to  
166 determine over-represented Kyoto Encyclopedia of Genes (KEGG) pathways and  
167 Genomes Gene Ontology (GO) categories. GO analysis demonstrated that 31.4% of  
168 genes were involved in signal transduction (Supplemental Table 1). As shown in Table  
169 1, phosphoinositide 3-kinase (PI3K)/Akt signaling pathway, neuroactive  
170 ligand-receptor interaction, mitogen-activated protein kinase (MAPK) signaling  
171 pathway, calcium signaling pathway, repressor activator protein 1 (Rap1) signaling  
172 pathway, cyclic guanosine monophosphate (cGMP)-protein kinase G (PKG) signaling  
173 pathway, and cyclic adenosine monophosphate (cAMP) signaling pathway were the  
174 top-ranked results of KEGG enrichment. It is noteworthy that ADP-mediated platelet  
175 activation via purinergic receptors included almost all signal transduction pathways  
176 shown in Table 1 [24][25]. Interestingly, among the 288 predicted targets of TMPZ on  
177 atherosclerosis, 190 proteins were also involved in the platelet activation process  
178 (Supplemental Table 2). Therefore, it was assumed that the anti-atherosclerosis  
179 potential of TMPZ could be largely attributed to its inhibition of purinergic  
180 receptor-dependent platelet activation, which involves signal transduction pathways  
181 such as PI3K/Akt. Based on the predicted result, clopidogrel, an anti-platelet drug  
182 widely used in the clinical application, was chosen as the positive control.

183 **Table 1** KEGG pathway enrichment analysis of DLDTI results

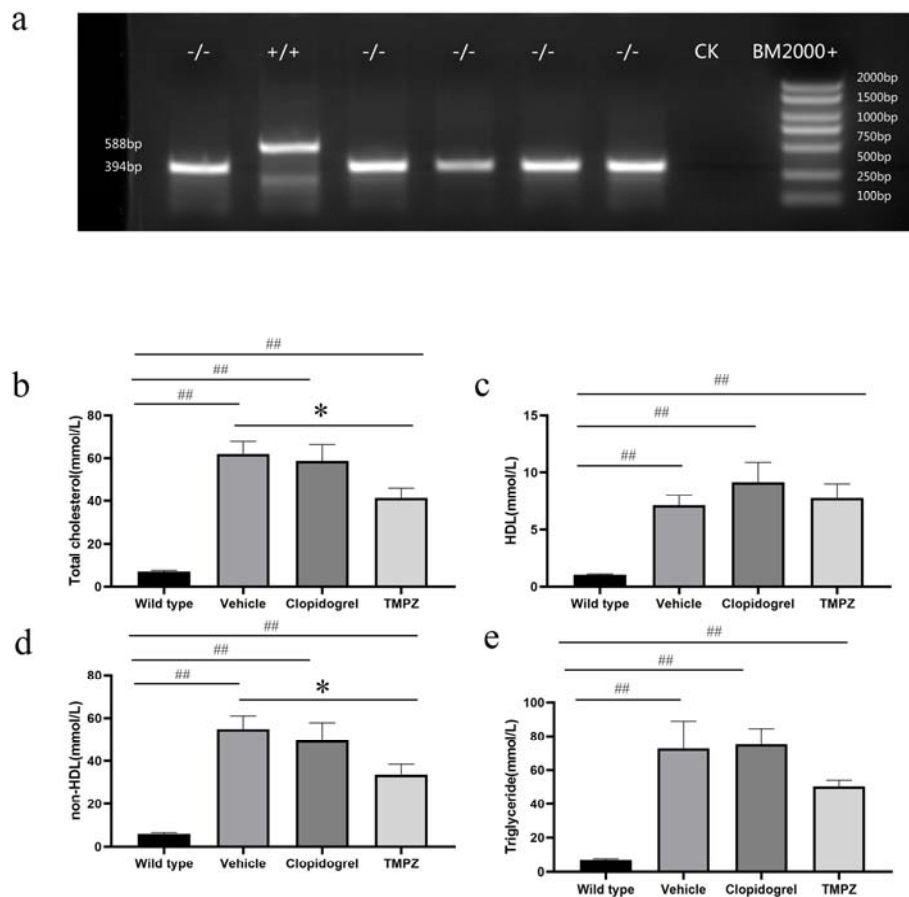
Class	KEGG term	Count	<i>P</i> value
Signal transduction	PI3K-Akt signaling pathway	36	2.49E-17
	Neuroactive ligand-receptor interaction	32	6.04E-17
	MAPK signaling pathway	29	1.08E-13
	Calcium signaling pathway	26	1.01E-15
	Rap1 signaling pathway	22	2.99E-11
	cGMP-PKG signaling pathway	20	2.99E-11
	cAMP signaling pathway	16	3.83E-07
Metabolism	Metabolism of xenobiotics by cytochrome P450	23	4.27E-20
	Steroid hormone biosynthesis	17	1.28E-14
	Retinol metabolism	15	5.89E-12
Immune system	Complement and coagulation cascades	21	3.06E-17
	Th17 cell differentiation	15	1.77E-09
Others	Regulation of actin cytoskeleton	16	6.90E-07
	Gap junction	15	2.74E-10
	Fluid shear stress and atherosclerosis	15	2.91E-08

184 **Validation**

185 **Ldlr<sup>-/-</sup> hamsters developed severe hyperlipidemia and atherosclerosis lesions**  
186 **when fed with HFHC diet**

187 Before dietary induction, genotypes were determined by PCR analysis. Using ear  
188 genomic DNA, 194-nucleotide deletion ( $\Delta$ 194) was detected in homozygous (-/-)  
189 hamsters (Figure 4a). After feeding them on high-fat and high-cholesterol (HFHF)

190 diet for 16 weeks, low-density lipoprotein receptor knock-out (*Ldlr*<sup>-/-</sup>) hamsters  
191 developed severe hyperlipidemia. As an antiplatelet medication, clopidogrel did not  
192 influence circulating levels of Total cholesterol (TC), triglyceride (TG), high-density  
193 lipoprotein (HDL) and non-HDL (Figure 4b, 4c, 4d and 4e). Compared with  
194 vehicle-treated hamsters, decreased levels of TC ( $p<0.05$ ) and non-HDL ( $p<0.05$ )  
195 were observed in TMPZ-treated group (Fig. 4b and 4d). However, TMPZ did not  
196 influence TG or HDL levels.



197

198 Figure 4. Genotyping and lipid parameters between different groups. (a).PCR analysis  
199 was performed using ear genomic DNA from WT (+/+) and homozygote (-/-) with  
200 the  $\Delta 194$  deletion. The concentrations of plasma TC (b), HDL(c), non-HDL(d) and  
201 TG(e) were measured in WT, vehicle, TMPZ and clodipogrel groups at the endpoint

202 of this experiment. Differences were assessed by unpaired student t's test or  
203 Mann-Whitney test. \*  $p < 0.05$  versus Vehicle, \*\* $p < 0.01$  versus Vehicle. ### $p < 0.01$   
204 versus WT. All data were expressed as mean  $\pm$  standard error (SEM)

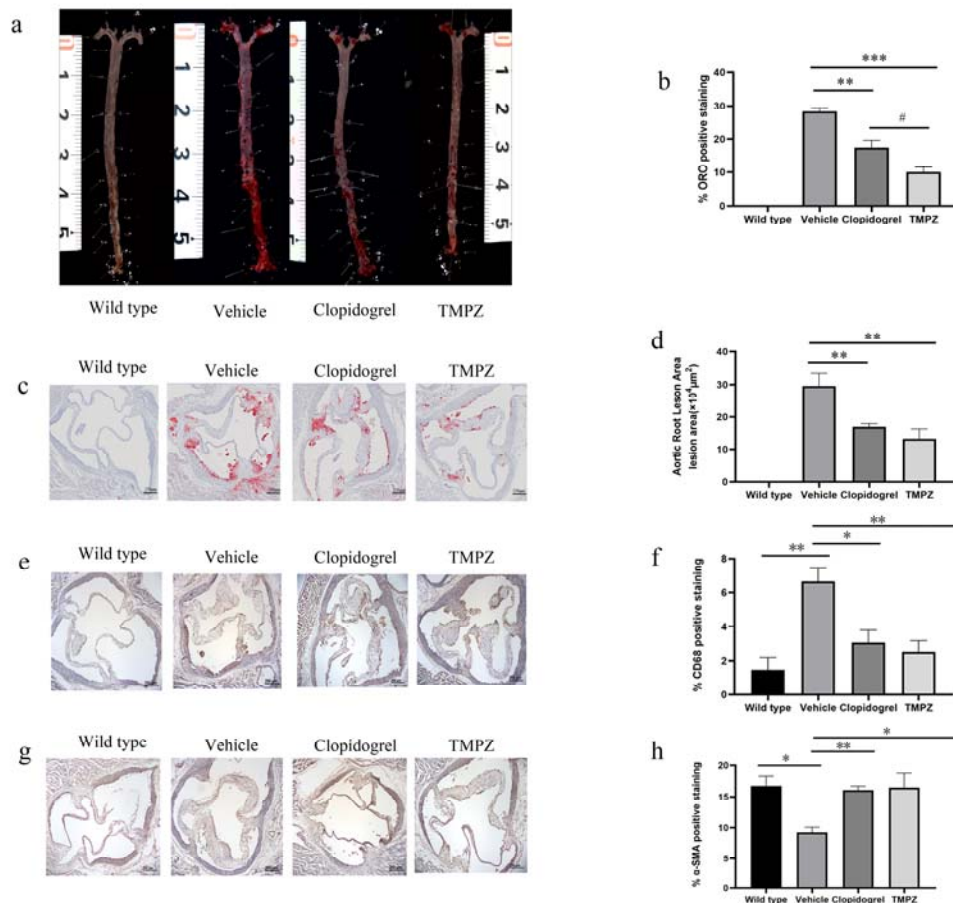
#### 205 **TMPZ ameliorated atherosclerosis lesion progression**

206 The *en face* analysis demonstrated that vehicle-treated hamsters developed significant  
207 atherosclerotic lesions (mean value 28.38%) throughout the whole aorta. However,  
208 atherosclerotic lesions induced by the same dietary manipulation in TMPZ- and  
209 clopidogrel-treated groups were significantly decreased (mean value 10.02% and  
210 mean value 17.47%, respectively) (Figure 5a and 5b). It's noteworthy that the lesion  
211 area in TMPZ-treated group was also less than that in clopidogrel-treated group  
212 (Figure 5b). As the blank control group, WT hamsters on chow diet did not develop  
213 any lesions throughout the aorta.

214 Similar to the *en face* analysis, the HFHC fed vehicle group had significantly  
215 increased lesion areas (mean area  $29.58 \times 10^4 \mu\text{m}^2$ ) in aortic roots compared to the  
216 blank controls measured by image analysis of Oil Red O staining, and either TMPZ  
217 (mean area  $13.25 \times 10^4 \mu\text{m}^2$ ) or clopidogrel (mean area  $16.99 \times 10^4 \mu\text{m}^2$ ) treatment  
218 reduced the lipid-rich areas (Figure 5c and 5d).

219 Under the stimulation of adhesion molecules, monocytes infiltrate into the intima and  
220 differentiate into macrophages [26]. Besides macrophage accumulation, diminished  
221 smooth muscle cells (SMC) could also exacerbate the formation of unstable plaques  
222 [27]. To determine the components of atherosclerosis lesions in the aortic root,  
223 immunohistochemical staining for macrophages and SMC was performed [28].  
224 Histopathological evaluation of macrophages accumulation revealed differences in  
225 CD68-positive areas between the groups. As shown in Figure 5e and 5f, the  
226 percentage of macrophage positive staining in lesions was increased by  
227 atherosclerosis progression in the vehicle-treated group. WT group (mean value  
228 1.48%) had significantly fewer macrophage accumulation than vehicle-treated group  
229 (mean value 6.65%). Infiltrated macrophages in lesions were significantly decreased

230 by TMPZ (mean value 2.52%) or clopidogrel (mean value 3.07%) treatment. As  
231 shown in Figure 5g and 5h, besides macrophage infiltration, the percentage of  $\alpha$ -SMA  
232 positive staining was diminished in *Ldlr*<sup>-/-</sup> hamsters (mean value 9.27%) compared  
233 with the WT hamsters (mean value 16.76%). Administration TMPZ (mean value  
234 16.50%) or clopidogrel (mean value 16.09%) for 8 weeks could ameliorate SMC  
235 reduction in atherosclerosis lesions.  
236



237  
238 Figure 5. Histological analysis. (a) Representative images of *en face* analysis. n=6.  
239 (b) Quantitative analysis of lesion areas in whole aortas. Differences were assessed by  
240 unpaired student t's test. (c) Representative images of Oil Red O staining of aortic  
241 root sections. (d) Quantitative analysis of lesion areas in aortic root sections. (e)  
242 Representative images of macrophage (CD68) analysis (b) Quantitative analysis of  
243 lesions area in macrophage analysis. (f) Representative images of SMC (SMA)

244 analysis (g) Quantitative analysis of lesions area in SMC. Differences were assessed  
245 by unpaired student t's test. \*  $p < 0.05$  versus Vehicle, \*\* $p < 0.01$  versus Vehicle.  
246 # $p < 0.05$  versus clopidogrel. Scale bar=250 $\mu$ m. n=3. All data were expressed as mean  
247  $\pm$ SEM.

#### 248 **TMPZ inhibited signaling transduction in ADP-mediated platelet activation**

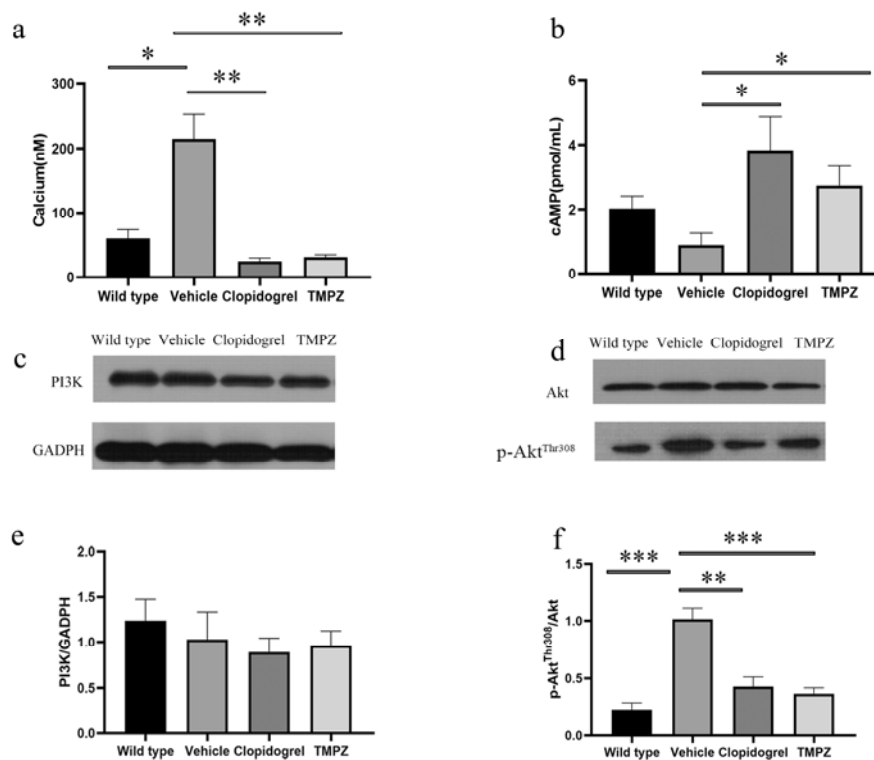
249 In addition to the surrogates of platelet activation, calcium and cAMP signaling are  
250 also essential in signal transduction. Downstream from Gq signaling, protein kinase C  
251 (PKC) activation results in the formation of inositol triphosphate (IP3), which leads to  
252 an elevation of intracellular calcium [24]. Calcium mobilization is also required for  
253 the phosphorylation of Akt (also known as protein kinase B) in PI3K/Akt signaling  
254 pathway [29]. In response to ADP, Gi signaling activation mediates the inhibition of  
255 AC, resulting in the diminished synthesis of cAMP. The inhibitory effect of Gi on  
256 cAMP synthesis could cause platelet activation [25].

257 Figure 6 shows that fura-2/AM is a membrane-permeant calcium indicator. The ratio  
258 of F340/F380 is directly correlated to the amount of intracellular calcium. The data  
259 revealed that TMPZ and clopidogrel markedly inhibited calcium mobilization, as  
260 detected using fluorescence mode of Synergy H1 microplate reader. Moreover,  
261 TMPZ-and clopidogrel-treated groups showed a higher concentration of cAMP in the  
262 active platelets. These findings indicate that TMPZ and clopidogrel could inhibit  
263 calcium mobilization and elevate intracellular concentration of cAMP, thereby  
264 inhibiting platelet activation.

265 As the major downstream effector of PI3K, Akt plays an essential role in the  
266 regulation of platelet activation. Stimulation of platelets with ADP could result in Akt  
267 activation, which was indicated by Akt phosphorylation [29]. The protein expressions  
268 of PI3K, Akt, and p-Akt in the top-ranked signal transduction pathway were measured  
269 to validate the predicted pathways. ADP-induced P2Y12 receptor activation could  
270 cause PI3K dependent Akt phosphorylation, a critical positive regulator pathway for  
271 signal amplification. There was no difference in PI3K expression levels between WT,



272 vehicle, TMPZ, and clopidogrel groups (Figure 6c). Phosphorylation of Akt was  
273 inhibited by TMPZ or clopidogrel administration when compared with vehicle-treated  
274 group. It is noteworthy that phosphorylation of Akt did not differ between WT, TMPZ  
275 and clopidogrel groups, which indicates that platelet activity in atherosclerosis  
276 hamsters treated with TMPZ or clopidogrel could be comparable to that in healthy  
277 ones (Figure 6d). These findings indicate that TMPZ and clopidogrel could attenuate  
278 Akt signaling, thereby blocking the platelet activation induced by  
279 ADP.



280  
281 **Figure 6.** Signaling transduction in ADP-mediated platelet activation. (a) Intracellular  
282 calcium concentration. (b) Intracellular cAMP concentration. Western blot analyses of  
283 the expression of PI3K (c), Akt (d) and p-Akt (d). Differences were assessed by  
284 unpaired student t's test with or without Welch's corrections. \*\*  $p < 0.01$  versus  
285 Vehicle, \*  $p < 0.05$  versus Vehicle.  $n = 4-6$ . All data were expressed as mean  $\pm$  SEM.

## 286 Discussion



287 In summary, this study provides a novel DTI model and validates its efficacy via a  
288 novel atherosclerosis model. This DLDTI model could provide an alternative to the  
289 high-throughput screening of drug targets. The proposed approach simultaneously  
290 fuses the topology of complex networks and diverse information from heterogeneous  
291 data sources and copes with the noisy, incomplete, and high-dimensional nature of  
292 large-scale biological data by learning the low-dimensional and rich depth features of  
293 drugs and proteins. The low-dimensional descriptors learned by DLDTI capture  
294 attribute characteristics, interaction information, relational properties, and network  
295 topology attributes of each drug or target node in a complex network. The  
296 low-dimensional feature vectors were used to train DLDTI to obtain the optimal  
297 mapping space and to infer new DTIs by ranking drug-target interaction candidates  
298 based on their proximity to the optimal mapping space. New DTIs were inferred by  
299 integrating drug- and protein-related multiple networks, to demonstrate DLDTI's  
300 ability to integrate heterogeneous information and that deep neural networks are  
301 capable of extracting drug and target networks and that deep features of attributes can  
302 effectively improve the prediction accuracy. This work also proved that TMPZ  
303 administration could attenuate atherosclerosis lesions, characterized by diminished  
304 lipid deposition, macrophage accumulation, and increased SMC percentage.  
305 Moreover, TMPZ could inhibit platelet activation by inhibiting Akt's phosphorylation  
306 and calcium mobilization and increasing intracellular cAMP concentration.

307 The current study proposes a learning-based framework called DLDTI for identifying  
308 the association of drug targets. The structural characteristics of drug and the  
309 characteristics of the protein properties were firstly extracted. An automatic  
310 encoder-based model was then proposed for feature selection. Using this feature  
311 representation, a convolutional neural network architecture was proposed for  
312 predicting the DTI. The advantages of DLDTI were demonstrated by comparing it  
313 with three different methods. Experiments on DTI showed that the performance of  
314 DLDTI was better than that of the alternative method, which shows that the proposed  
315 learning-based framework was properly designed.

316 Furthermore, in the validation study of the DLDTI model, we used TMPZ (a drug  
317 with known structure) to explore its effects on atherosclerosis in vivo. Consistent with  
318 previous studies [16][17][18], the results revealed that TMPZ could ameliorate the  
319 phenotyping of atherosclerosis in *Ldlr*<sup>-/-</sup> hamsters, a novel atherosclerosis model  
320 [30][31]. Diminished lipid deposition and macrophage accumulation, and increased  
321 percentage of SMC were observed in TMPZ- and clopidogrel-treated hamsters, in  
322 comparison with vehicle-treated animals. Interestingly, it was found that the majority  
323 of potential pathways of TMPZ on atherosclerosis were also involved in signal  
324 transduction of platelet activation. From the initial endothelial dysfunction in the early  
325 stage to the destabilized plaques in the advanced stage, platelet plays a pivotal role  
326 [32]. Activated platelets act as the key trigger for rupture-prone plaque formation.  
327 Current evidence shows that platelet hyperactivity is associated with a prothrombotic  
328 state and increases the incidence of recurrent cardiovascular events among patients  
329 with coronary artery disease [33]. Over the past decade, it has been found that  
330 platelets can be activated by various stimuli like collagen, thrombin, and ADP. Based  
331 on the pathway analysis of predicted results, this work focused on signal transduction  
332 in ADP-mediated platelet activation (Table 1). The results revealed that the activated  
333 signal transductions, characterized by increased calcium mobilization, decreased  
334 cAMP concentration and increased phosphorylation of Akt were observed in ex vivo  
335 platelets from vehicle-treated hamsters. Platelets from TMPZ- and clopidogrel-treated  
336 hamsters showed increased cAMP level and diminished calcium mobilization and  
337 phosphorylation of Akt.

338 Future studies will focus on solving “cold-start” problem, which is faced by all  
339 algorithms that apply collaborative filtering technology. In the current study, the top  
340 three feature vectors with the highest scores are weighted by 60%, 30%, and 10%,  
341 respectively, based on the similarity of protein sequences and the similarity of drug  
342 structures, to obtain new interaction feature vectors to solve the cold start problem. In  
343 addition, to validate the study, the top-ranked pathways of signal transduction  
344 involved in platelet activation were examined, although reduced TC and non-HDL

345 levels and diminished macrophage accumulation in lesions were also observed. These  
346 effects also could also contribute to the diminished total lesions area and be the topic  
347 of our following research.

## 348 **Materials and Methods**

### 349 **Prediction experiments**

#### 350 **Human drug-target interactions database**

351 The current study used the DrugBank (<http://www.drugbank.ca>) established by  
352 Wishart *et al.* as the benchmark [34]. The chemical structure of each drug in SMILES  
353 format was extracted from the DrugBank. This study used drugs that satisfied the  
354 human target represented by a unique EnsemblProt login number. In summary, 904  
355 drugs and 613 unique human targets (proteins) were linked to construct a drug-target  
356 interaction network  $A$  of positive samples, while a matching number of unknown  
357 drug-target pairs (by excluding all known DTIs) was randomly selected as negative  
358 samples.

#### 359 **Feature representation**

360 **Gaussian interaction profile kernel similarity for drugs and targets.** According to  
361 previous studies, drug similarity can be determined by calculating their nuclear  
362 similarity through Gaussian interaction profile kernel similarity (GIP) [35][36]. The  
363 GIP similarity between drug  $d_i$  and drug  $d_j$  is defined as follow:

$$D_{sim}(d_i, d_j) = \exp\left(-\tau_d \cdot \|V(d_i) - V(d_j)\|^2\right) \quad (1)$$

364

365 Where, the binary vector  $V(d_i)$  and  $V(d_j)$  are the  $i$ -th and  $j$ -th row vectors of the  
366 drug-target interaction network  $A$ .  $\tau_d$  is the kernel bandwidth and is computed by  
367 normalizing the original parameter  $\tau_d'$ :

$$\tau_d = \frac{\tau'_d}{\frac{1}{n_d} \sum_{i=1}^{n_d} \|V(d_i)\|^2} \quad (2)$$

368

369 Similarly, the GIP similarity for targets can be defined as follows:

$$D_{sim}(d_i, d_j) = \exp\left(-\tau_d * \|V(p_i) - V(p_j)\|^2\right) \quad (3)$$

370

371 Where, the binary vector  $V(p_i)$  and  $V(p_j)$  are the  $i$ -th row and the  $j$ -th column

372 vector of the drug-target interaction network  $A$ , respectively.  $\tau_p$  is the kernel

373 bandwidth and is computed by normalizing the original parameter  $\tau'_p$ :

$$\tau_p = \frac{\tau'_p}{\frac{1}{n_p} \sum_{i=1}^{n_p} \|V(p_i)\|^2} \quad (4)$$

374

375 **Protein sequence feature.** The sequences for drug targets (proteins) in Homo sapiens

376 were downloaded from STRING. The  $k$ -mer algorithm was used to count

377 Subsequence information in protein sequences and used as a feature vector to solve

378 alignment issues presented by differences in sequence length [37].

379 **Drug structure feature.** Morgan and circular fingerprints were used to map the

380 structure information of drugs to feature vectors based on SMILES for drugs

381 downloaded from the DrugBank database.

382 **Graph embedding-based feature for drugs and targets.** Graph data is rich in

383 behavioral information about nodes, which can be used as a comprehensive descriptor

384 for drugs and targets [38]. To map a high-dimensional dense matrix like graph data to

385 a low-density vector, a Graph Factorization algorithm [39] was hereby introduced.  
386 Graph factorization (GF) is a method for graph embedding with time complexity  
387  $O(|E|)$ . To obtain the embedding, GF factorizes the adjacency matrix of the graph to  
388 minimize loss functions as follow:

$$s(P, Q, \lambda) = \frac{1}{2} \sum_{(i,j) \in E} (P_{ij} - \langle Q_i, Q_j \rangle)^2 + \frac{\lambda}{2} \sum_i \|Q_i\|^2 \quad (5)$$

389

390 Where,  $\lambda$  is the regularization coefficient.  $P$  and  $Q$  are the adjacency matrix with  
391 weights and factor matrix, respectively.  $E$  is the set of edges, which includes  $i$  and  $j$ .

392 The gradient of the function  $s$  with respect to  $Q_i$  is defined as follow:

$$\frac{\partial s}{\partial Q_i} = - \sum_{k \in N_o} (P_{kj} - \langle Q_k, Q_j \rangle) Q_j + \lambda Q_i \quad (6)$$

393

394 Where,  $N_o$  is the set of neighbors of node  $o$  and the Graph Factorization algorithm,  
395 graph embeddings and targets in the drug-target interaction network can be obtained  
396 to describe their behavioral information.

### 397 **Stacked Autoencoder**

398 Since DLDTI integrates heterogeneous data from multiple sources, including protein  
399 sequence, drug structure, and drug-target interaction network information, the  
400 integrated biological data is characterized by noise, incompleteness and has  
401 high-dimension. Therefore, stack autoencoder (SAE) was used to establish the  
402 optimal mapping of drug space to target space to obtain low dimensional drug Feature  
403 vector [40][41]. SAE can be defined as follows:

$$y = f(x) = S_e(Wx + b) \quad (7)$$

404

$$\mathbf{z} = g(\mathbf{y}) = S_a(W\mathbf{x} + \mathbf{b}') \quad (8)$$

405

406 Where  $\mathbf{y}$  and  $\mathbf{z}$  are encoding and decoding function, respectively.  $W$  and  $W'$  are

407 the relational parameters between two layers, respectively.  $\mathbf{b}$  and  $\mathbf{b}'$  are vectors of

408 bias parameters. The activation function used is ReLU:

$$S_a(t) = S_a(t) = \max(0, W^T + b) \quad (9)$$

409

#### 410 Convolutional neural network

411 Convolutional neural networks were proposed by Lecun *et al.* in 1989[42].

412 Subsequently, they have performed well in image classification, sentence

413 classification, and biological data analysis. In this study, convolutional neural

414 networks were used to train supervised learning models to predict potential

415 drug-target interactions. They were also chosen as supervised learning models to

416 study deep features and predict potential drug targets interaction. The model used has

417 convolutional and activation, Maxpooling, fully connected and softmax layers. Their

418 roles are to extract depth features, down-sample, and classify samples, respectively.

419 The convolutional layer is one of the most important parts of the CNN and aims to

420 learn the deep characteristics of the input vectors, which is defined as follows;

$$C_m = \sum_{i=1}^{N_k} W_i X_{m+i} \quad (10)$$

421

422 Where;  $X$  is the input feature of length  $L$ ,  $N_k$  is the number of kernels,

423  $m \in \{0, \dots, L - N\}$ , and  $W$  is a weight vector of length  $N_k$ . The feature map  $C_m$  is

424 then put into the activation function ReLU, which is defined as follow:

425  $f(x) = \max(0, x)$  (11)

426 The ReLU function increases the nonlinear relationship between the layers of the  
427 neural network, saves computation, solves the problem of gradient disappearance, and  
428 reduces the interdependence of parameters to mitigate the problem of overfitting.

429 The convolutional and maximum pooling layers can extract important features from  
430 the input vectors. The output of all kernels was then concatenated into a vector and  
431 fed to the fully-connected layer  $f(W \cdot y)$ . Where;  $y$  is the output of Maxpooling  
432 layer and  $W$  is the weight matrix. Finally, the softmax layer scored the input vectors  
433 as a percentage.

#### 434 **Pathway analysis of predicted results from DLDTI**

435 Atherosclerosis-related gene sets were downloaded from GeneCards  
436 (<https://www.genecards.org/>) [43]. After using retrieve tool on Uniprot database  
437 (<https://www.uniprot.org/>), different identifiers from Drug Bank and GeneCards were  
438 converted to UniProtKB. Based on intersection of potential targets of TMPZ from  
439 DLDTI model and confirmed target proteins of atherosclerosis, the matched targets  
440 were regarded as the predicted targets of TMPZ on atherosclerosis. The predicted  
441 targets were uploaded to STRING for KEGG pathway and GO analysis.

#### 442 **Validation experiments**

##### 443 **Ldlr<sup>-/-</sup> hamsters**

444 This study was approved by the Animal Ethics Committee of Xiyuan Hospital and  
445 strictly adhered to the principles of laboratory animal care (NIH publication  
446 No.85Y23, revised 1996). Male, 8-week aged and Ldlr<sup>-/-</sup> hamsters were provided by  
447 the health science center, Peking University. The Ldlr<sup>-/-</sup> genotype was confirmed  
448 using polymerase chain reaction analysis of DNA extracts from ears [31]. After one  
449 week of acclimatization, they were fed on HCHF diet containing 15% lard and 0.5%  
450 cholesterol (Biotech company, China) for eight weeks. The Ldlr<sup>-/-</sup> hamsters were then

451 randomly divided into three groups according to their weights (n=8 per group) and  
452 orally administered with a mixture of volume vehicle (distilled water),  
453 tetramethylpyrazine (32mg/kg/d) and clopidogrel (32mg/kg/d) drugs for eight weeks.  
454 Wild type golden Syrian hamsters (n=8) purchased from Vital River Laboratory  
455 (Charles River, Beijing, China) were fed on a standard chow diet as healthy control.  
456 All hamsters were maintained on a 12-hour light/12-hour dark cycle with free access  
457 to water.

458 Finally, the hamsters were fasted for 12h and anesthetized through intraperitoneal  
459 injection of 1% sodium phenobarbital (70mg/kg). Blood samples were taken from  
460 abdominal aortas, and plasma was separated by centrifugation for 10 min at 2700×g.  
461 TC, TG, and HDL were determined using commercially available kits (BIOSINO,  
462 China).

#### 463 **Oil red O staining**

464 As described previously [31][44], anesthetized hamsters were perfused with 0.01M  
465 PBS through the left ventricle. In brief, hearts and whole aortas were placed in 4%  
466 paraformaldehyde solution overnight and transferred to 20% sucrose solution for one  
467 week. Hearts were then fixed into OCT compound and cross-sectioned (8 um per  
468 slice). The atherosclerotic lesions in aortic root were stained with 0.3% Oil red O  
469 solution (Solarbio, China), rinsed with 60% isopropanol and distilled water and  
470 counterstained with hematoxylin. The results were represented by the percentage  
471 positive area of total area (en face analysis) and net lesion area (aortic root sections).  
472 Images were analyzed with Image J [45].

#### 473 **Immunohistochemistry analysis**

474 Analysis of atherosclerotic plaque cell composition was determined by  
475 immunohistochemistry analysis of the aortic root. Macrophages and SMC were  
476 stained with CD68 (BOSTER, BA36381:100) antibody and a-SMA antibody  
477 (BOSTER, A03744, 1:100), as reported previously in hamster researches [31]. Then  
478 biotinylated second antibody (Vector Laboratories, ABC Vectastain, 1:200) were used  
479 for incubation under 2% normal blocking serum. The cryosections were visualized



480 using 3,3-diaminobenzidine (Vector Laboratories, DAB Vectastain). The results were  
481 represented by the percentage positive area of the total cross-sectional vessel wall  
482 area in the aortic root sections and analyzed using Image J [45].

#### 483 **Washed platelet preparation**

484 Blood per hamster, 3 to 4 mL was collected from abdominal aortas into a tube  
485 containing an acid-citrate-dextrose anticoagulant (83.2mM D-glucose, 85mM  
486 trisodium citrate dihydrate, 19mM citric acid monohydrate, pH5.5). Platelet-rich  
487 plasma (PRP) was prepared after centrifugation at 300×g for 10min in room  
488 temperature. For washed platelet preparation, PRP was centrifuged at 1500×g for  
489 2min. After collecting supernatant consisting of platelet-poor plasma into another  
490 centrifuge tube, the remaining PRP was washing three times, and the pellet was  
491 re-suspended in a modified Tyrode buffer (2.4mM HEPES, 6.1mM D-glucose,  
492 137mM NaCl, 12mM  $\text{NaHCO}_3$ , 2.6mM KCl, pH7.4).

#### 493 **Assessment of platelet activity**

494 Washed platelets were loaded with fura-2/AM(5μM, Molecular Probe) in the presence  
495 of Pluronic F-127 (0.2μg/mL, Molecular Probe) and then incubated at 37°C for 1 hour  
496 in the dark [46]. Platelets were washed and re-suspended in Tyrode buffer containing  
497 1mM calcium. After activation of ADP (20μM, Sigma), intracellular calcium  
498 concentration was measured using a fluorescence mode of Synergy H1 microplate  
499 reader (Biotek, USA). Excitation wavelengths was alternated at 340 and 380 nm.  
500 Excitation was measured at 510 nm. TritonX-100 and EGTA were used for calibration  
501 of maximal and minimal calcium concentrations, respectively. Washed platelets were  
502 activated by ADP and then lysed by 0.1M HCl on ice. According to the  
503 manufacturer's instructions, the level of intracellular cAMP was determined by  
504 ELISA (Enzo Life Sciences, ADI-900-066).

#### 505 **Western blot analysis**

506 Washed platelets from each group were lysed with radioimmunoprecipitation assay  
507 (RIPA) buffer with the presence of protease and phosphatase inhibitor mixtures on ice  
508 (Solarbio, China). Lysates were separated by 10000×g centrifugation for 10 min at 4°C.

509 Total protein concentrations were determined by BCA method. Equal amounts of total  
510 protein (40µg) were resolved in SDS-PAGE and electroblotted. The nitrocellulose  
511 membranes were blocked with 5% skimmed milk at room temperature for 2 hours and  
512 incubated with primary antibodies targeting PI3K(CST, 4257T, 1:500), Akt(CST,  
513 9272, 1:2000), p-Akt(CST,2965,1:1000) and GADPH (Abcam, ab8245, 1:5000)  
514 overnight at 4°C. The membranes were then incubated with the HRP-conjugated  
515 anti-rabbit antibody for 1 hour at 37°C, followed by enhanced chemiluminescence  
516 detection.

### 517 **Statistical analysis**

518 All data were expressed as mean ±standard error (SEM). Shapiro-Wild test and  
519 Levene's test were used for determining normality of data distribution and  
520 homogeneity of variances, respectively. An unpaired student's t-test was used to  
521 compare data among different groups when data were normally distributed, and  
522 variances were equal among the groups. Unpaired t test with Welch's correction was  
523 used when there was unequal standard deviation among groups. Mann-Whitney test  
524 was used for nonparametric test. All p-values less than 0.05 were considered  
525 statistically significant. All statistical analyses were performed using GraphPad Prism  
526 8.0 (GraphPad, United states).

### 527 **Author contributions**

528 Y.Z. and D.Z.S. spearheaded and supervised all the experiments. Y.Z., D.Z.S., Y.H.Z.  
529 and K.Z. designed research. Y.H.Z, K.Z., B.Y.G., L.S., M.M.G., Y.H.W., and J.G.  
530 conducted experiments. L.S. and B.Y.G. analyzed data. Y.H.Z, K.Z., and Y.Z. prepared  
531 the manuscript. All authors reviewed and approved the manuscript.

### 532 **Disclosure of Potential Conflicts**

533 The authors declare that none of them have any conflict of interest.

### 534 **Acknowledgements**

535 This work was funded by the National Natural Science Foundation of China, grant  
536 (No. 81703927) and the Fundamental Research Funds for the Central public welfare  
537 research institutes of China, grant (No. ZZ13-YQ-008). The images of atherosclerosis

538 and platelets in the graphical abstract were adapted from Servier Medical Art  
539 (<http://smart.servier.com>). Dr. Jerry, a professional English editor, provided language  
540 help and writing assistance.

#### 541 **References**

- 542 [1] Avorn J. The \$2.6 billion pill - Methodologic and policy considerations. *N.*  
543 *Engl. J. Med.*, vol. 372, 2015, p. 1877–9.  
544 <https://doi.org/10.1056/NEJMp1500848>.
- 545 [2] Munos B. Lessons from 60 years of pharmaceutical innovation. *Nat Rev Drug*  
546 *Discov* 2009;8:959–68. <https://doi.org/10.1038/nrd2961>.
- 547 [3] Nowak-Sliwinska P, Scapozza L, Altaba AR i. Drug repurposing in oncology:  
548 Compounds, pathways, phenotypes and computational approaches for  
549 colorectal cancer. *Biochim Biophys Acta - Rev Cancer* 2019;1871:434–54.  
550 <https://doi.org/10.1016/j.bbcan.2019.04.005>.
- 551 [4] Sleire L, Førde-Tislevoll HE, Netland IA, Leiss L, Skeie BS, Enger PØ. Drug  
552 repurposing in cancer. *Pharmacol Res* 2017;124:74–91.  
553 <https://doi.org/10.1016/j.phrs.2017.07.013>.
- 554 [5] Ianculescu I, Weisman MH. The role of methotrexate in psoriatic arthritis:  
555 What is the evidence? *Clin Exp Rheumatol* 2015;33:94–7.
- 556 [6] Corbett A, Smith J, Ballard C. New and emerging treatments for Alzheimers  
557 disease. *Expert Rev Neurother* 2012;12:535–43.  
558 <https://doi.org/10.1586/ern.12.43>.
- 559 [7] Santos R, Ursu O, Gaulton A, Bento AP, Donadi RS, Bologa CG, et al. A  
560 comprehensive map of molecular drug targets. *Nat Rev Drug Discov*  
561 2016;16:19–34. <https://doi.org/10.1038/nrd.2016.230>.
- 562 [8] Duran C, Daminelli S, Thomas J, Joachim Haupt V, Schroeder M, Cannistraci  
563 CV. Pioneering topological methods for network-based drug-target prediction  
564 by exploiting a brain-network self-organization theory. *Brief Bioinform*  
565 2017;19:1183–202. <https://doi.org/10.1093/bib/bbx041>.
- 566 [9] Luo Y, Zhao X, Zhou J, Yang J, Zhang Y, Kuang W, et al. A network

- 567 integration approach for drug-target interaction prediction and computational  
568 drug repositioning from heterogeneous information. *Nat Commun* 2017;8.  
569 <https://doi.org/10.1038/s41467-017-00680-8>.
- 570 [10] Zeng X, Zhu S, Lu W, Liu Z, Huang J, Zhou Y, et al. Target identification  
571 among known drugs by deep learning from heterogeneous networks. *Chem Sci*  
572 2020;11:1775–97. <https://doi.org/10.1039/c9sc04336e>.
- 573 [11] Bleakley K, Yamanishi Y. Supervised prediction of drug-target interactions  
574 using bipartite local models. *Bioinformatics* 2009;25:2397–403.  
575 <https://doi.org/10.1093/bioinformatics/btp433>.
- 576 [12] Mei JP, Kwok CK, Yang P, Li XL, Zheng J. Drug-target interaction prediction  
577 by learning from local information and neighbors. *Bioinformatics*  
578 2013;29:238–45. <https://doi.org/10.1093/bioinformatics/bts670>.
- 579 [13] Gönen M. Predicting drug-target interactions from chemical and genomic  
580 kernels using Bayesian matrix factorization. *Bioinformatics* 2012;28:2304–10.  
581 <https://doi.org/10.1093/bioinformatics/bts360>.
- 582 [14] Wan F, Hong L, Xiao A, Jiang T, Zeng J. NeoDTI: Neural integration of  
583 neighbor information from a heterogeneous network for discovering new  
584 drug-target interactions. *Bioinformatics* 2019;35:104–11.  
585 <https://doi.org/10.1093/bioinformatics/bty543>.
- 586 [15] Guo M, Liu Y, Shi D. Cardiovascular Actions and Therapeutic Potential of  
587 Tetramethylpyrazine (Active Component Isolated from *Rhizoma Chuanxiong*):  
588 Roles and Mechanisms. *Biomed Res Int* 2016;2016.  
589 <https://doi.org/10.1155/2016/2430329>.
- 590 [16] Duan J, Xiang D, Luo H, Wang G, Ye Y, Yu C, et al. Tetramethylpyrazine  
591 suppresses lipid accumulation in macrophages via upregulation of the  
592 ATP-binding cassette transporters and downregulation of scavenger receptors.  
593 *Oncol Rep* 2017;38:2267–76. <https://doi.org/10.3892/or.2017.5881>.
- 594 [17] Zhang Y, Ren P, Kang Q, Liu W, Li S, Li P, et al. Effect of  
595 tetramethylpyrazine on atherosclerosis and SCAP/SREBP-1c signaling

- 596 pathway in ApoE<sup>-/-</sup> mice fed with a high-fat diet. Evidence-Based  
597 Complement Altern Med 2017;2017. <https://doi.org/10.1155/2017/3121989>.
- 598 [18] Jiang F, Qian J, Chen S, Zhang W, Liu C. Ligustrazine improves  
599 atherosclerosis in rat via attenuation of oxidative stress. Pharm Biol  
600 2011;49:856–63. <https://doi.org/10.3109/13880209.2010.551776>.
- 601 [19] Libby P, Buring JE, Badimon L, Hansson GK, Deanfield J, Bittencourt MS, et  
602 al. Atherosclerosis. Nat Rev Dis Prim 2019;5:1–18.  
603 <https://doi.org/10.1038/s41572-019-0106-z>.
- 604 [20] Guo G, Wang H, Bell D, Bi Y, Greer K. KNN model-based approach in  
605 classification. Lect Notes Comput Sci (Including Subser Lect Notes Artif Intell  
606 Lect Notes Bioinformatics) 2003;2888:986–96.  
607 [https://doi.org/10.1007/978-3-540-39964-3\\_62](https://doi.org/10.1007/978-3-540-39964-3_62).
- 608 [21] Svetnik V, Liaw A, Tong C, Christopher Culberson J, Sheridan RP, Feuston  
609 BP. Random Forest: A Classification and Regression Tool for Compound  
610 Classification and QSAR Modeling. J Chem Inf Comput Sci 2003;43:1947–58.  
611 <https://doi.org/10.1021/ci034160g>.
- 612 [22] Freund Y, Schapire RE. A Decision-Theoretic Generalization of On-Line  
613 Learning and an Application to Boosting. J Comput Syst Sci 1997;55:119–39.  
614 <https://doi.org/10.1006/jcss.1997.1504>.
- 615 [23] Szklarczyk D, Gable AL, Lyon D, Junge A, Wyder S, Huerta-Cepas J, et al.  
616 STRING v11: Protein-protein association networks with increased coverage,  
617 supporting functional discovery in genome-wide experimental datasets.  
618 Nucleic Acids Res 2019;47:D607–13. <https://doi.org/10.1093/nar/gky1131>.
- 619 [24] Offermanns S. Activation of platelet function through G protein-coupled  
620 receptors. Circ Res 2006;99:1293–304.  
621 <https://doi.org/10.1161/01.RES.0000251742.71301.16>.
- 622 [25] Ballerini P, Dovizio M, Bruno A, Tacconelli S, Patrignani P. P2Y<sub>12</sub> receptors  
623 in tumorigenesis and metastasis. Front Pharmacol 2018;9:1–8.  
624 <https://doi.org/10.3389/fphar.2018.00066>.

- 625 [26] Geovanini GR, Libby P. Atherosclerosis and inflammation: Overview and  
626 updates. *Clin Sci* 2018;132:1243–52. <https://doi.org/10.1042/CS20180306>.
- 627 [27] Otsuka F, Yasuda S, Noguchi T, Ishibashi-Ueda H. Pathology of coronary  
628 atherosclerosis and thrombosis. *Cardiovasc Diagn Ther* 2016;6:396–408.  
629 <https://doi.org/10.21037/cdt.2016.06.01>.
- 630 [28] Liu X, Li J, Liao J, Wang H, Huang X, Dong Z, et al. Gpihbp1 deficiency  
631 accelerates atherosclerosis and plaque instability in diabetic Ldlr  $-/-$  mice.  
632 *Atherosclerosis* 2019;282:100–9.  
633 <https://doi.org/10.1016/j.atherosclerosis.2019.01.025>.
- 634 [29] Xiang B, Zhang G, Liu J, Morris AJ, Smyth SS, Gartner TK, et al. A  
635 Gi-independent mechanism mediating Akt phosphorylation in platelets. *J*  
636 *Thromb Haemost* 2010;8:2032–41.  
637 <https://doi.org/10.1111/j.1538-7836.2010.03969.x>.
- 638 [30] Zhao Y, Qu H, Wang Y, Xiao W, Zhang Y, Shi D. Small rodent models of  
639 atherosclerosis. *Biomed Pharmacother* 2020;129:110426.  
640 <https://doi.org/10.1016/j.biopha.2020.110426>.
- 641 [31] Guo X, Gao M, Wang Y, Lin X, Yang L, Cong N, et al. LDL Receptor  
642 Gene-ablated Hamsters: A Rodent Model of Familial Hypercholesterolemia  
643 With Dominant Inheritance and Diet-induced Coronary Atherosclerosis.  
644 *EBioMedicine* 2018;27:214–24. <https://doi.org/10.1016/j.ebiom.2017.12.013>.
- 645 [32] Fuentes EQ, Fuentes FQ, Andrés V, Pello OM, De Mora JF, Palomo IG. Role  
646 of platelets as mediators that link inflammation and thrombosis in  
647 atherosclerosis. *Platelets* 2013;24:255–62.  
648 <https://doi.org/10.3109/09537104.2012.690113>.
- 649 [33] Freynhofer MK, Iliev L, Bruno V, Rohla M, Egger F, Weiss TW, et al. Platelet  
650 turnover predicts outcome after coronary intervention. *Thromb Haemost*  
651 2017;117:923–33. <https://doi.org/10.1160/TH16-10-0785>.
- 652 [34] Wishart DS, Feunang YD, Guo AC, Lo EJ, Marcu A, Grant JR, et al.  
653 DrugBank 5.0: A major update to the DrugBank database for 2018. *Nucleic*

- 654 Acids Res 2018;46:D1074–82. <https://doi.org/10.1093/nar/gkx1037>.
- 655 [35] Zheng K, Wang L, You ZH. CGMDA: An Approach to Predict and Validate  
656 MicroRNA-Disease Associations by Utilizing Chaos Game Representation and  
657 LightGBM. IEEE Access 2019;7:133314–23.  
658 <https://doi.org/10.1109/ACCESS.2019.2940470>.
- 659 [36] Zheng K, You ZH, Wang L, Li YR, Wang Y Bin, Jiang HJ. MISSIM:  
660 Improved miRNA-Disease Association Prediction Model Based on Chaos  
661 Game Representation and Broad Learning System. vol. 11645 LNAI. Springer  
662 International Publishing; 2019. [https://doi.org/10.1007/978-3-030-26766-7\\_36](https://doi.org/10.1007/978-3-030-26766-7_36).
- 663 [37] Zheng K, You ZH, Li JQ, Wang L, Guo ZH, Huang YA. iCDA-CGR:  
664 Identification of circRNA-disease associations based on Chaos Game  
665 Representation. PLoS Comput Biol 2020;16:e1007872.  
666 <https://doi.org/10.1371/journal.pcbi.1007872>.
- 667 [38] Zheng K, You Z, Wang L, Wong L, Chen Z. Inferring Disease-Associated  
668 Piwi-Interacting RNAs via Graph Attention Networks 2020:1–7.
- 669 [39] Ahmed A, Shervashidze N, Narayanamurthy S, Josifovski V, Smola AJ.  
670 Distributed large-scale natural graph factorization. WWW 2013 - Proc. 22nd  
671 Int. Conf. World Wide Web, 2013, p. 37–47.  
672 <https://doi.org/10.1145/2488388.2488393>.
- 673 [40] Shin HC, Orton MR, Collins DJ, Doran SJ, Leach MO. Stacked autoencoders  
674 for unsupervised feature learning and multiple organ detection in a pilot study  
675 using 4D patient data. IEEE Trans Pattern Anal Mach Intell 2013;35:1930–43.  
676 <https://doi.org/10.1109/TPAMI.2012.277>.
- 677 [41] Zheng K, You ZH, Wang L, Zhou Y, Li LP, Li ZW. MLMDA: A machine  
678 learning approach to predict and validate MicroRNA-disease associations by  
679 integrating of heterogenous information sources. J Transl Med 2019;17:1–14.  
680 <https://doi.org/10.1186/s12967-019-2009-x>.
- 681 [42] Yann L, Yoshua B. Convolutional Networks for Images, Speech, and  
682 Time-Series 1995;4:2571–5. <https://doi.org/10.1109/IJCNN.2004.1381049>.

- 683 [43] Stelzer G, Rosen N, Plaschkes I, Zimmerman S, Twik M, Fishilevich S, et al.  
684 The GeneCards suite: From gene data mining to disease genome sequence  
685 analyses. *Curr Protoc Bioinforma* 2016;2016:1.30.1-1.30.33.  
686 <https://doi.org/10.1002/cpbi.5>.
- 687 [44] Liu X, Li J, Liao J, Wang H, Huang X, Dong Z. Gpibp1 deficiency  
688 accelerates atherosclerosis and plaque instability in 2019;282:100–9.  
689 <https://doi.org/10.1016/j.atherosclerosis.2019.01.025>.
- 690 [45] Kuzuya M, Nakamura K, Sasaki T, Xian WC, Itohara S, Iguchi A. Effect of  
691 MMP-2 deficiency on atherosclerotic lesion formation in apoE-deficient mice.  
692 *Arterioscler Thromb Vasc Biol* 2006;26:1120–5.  
693 <https://doi.org/10.1161/01.ATV.0000218496.60097.e0>.
- 694 [46] Pleines I, Elvers M, Strehl A, Pozgajova M, Varga-szabo D, May F, et al. Rac1  
695 is essential for phospholipase C-  $\gamma$  2 activation in platelets 2009:1173–85.  
696 <https://doi.org/10.1007/s00424-008-0573-7>.

## 697 **Figure legends**

698 **Figure 1.** The flowchart of the DLDTI pipeline. DLDTI first integrates a variety of  
699 drug-related information sources to construct a heterogeneous network and applies a  
700 compact feature learning algorithm to obtain a low-dimensional vector representation  
701 of the features describing the topological properties for each node. Next, DLDTI  
702 determines the optimal mapping from the plenary mapping space to the prediction  
703 subspace, and whether the feature vector is close to the known correlations.  
704 Afterwards, DLDTI infers the new DTIs by ranking the drug-target interaction  
705 candidates according to their proximity to the predicted subspace

706 **Figure 2.** Schematic illustration of compact feature learning. The Node2Vec  
707 algorithm is firstly used to calculate the topology information in complex networks.  
708 Gaussian interaction profile kernel similarity (GIP) and drug structure information are  
709 then extracted by a stacked automatic encoder, and the heterogeneous information is  
710 integrated to obtain a low-dimensional representation of the feature vector of each  
711 node. The resulting low-dimensional descriptor integrates the attribute characteristics,



712 interaction information, relationship attributes and network topology of each protein  
713 or target node in the complex network.

714 **Figure 3.** Performance of DLDTI. (a) ROC curves performed by DLDTI model on  
715 DrugBank dataset. (b) PR curves performed by DLDTI model on DrugBank dataset.  
716 (c) Performance comparison (AUC scores) among four different prediction model  
717 which are DTI-ADA, DTI-KNN, and DTI-RF.(d)Performance comparison (AUPR  
718 scores) among four different prediction models including DTI-ADA, DTI-KNN, and  
719 DTI-RF.(e)Performance comparison (Acc., F1, Pre., Rec. scores) among DTI-ADA,  
720 DTI-KNN, and DTI-RF prediction models.

721 **Figure 4.** Genotyping and lipid parameters between different groups. (a).PCR  
722 analysis was performed using ear genomic DNA from WT (+/+) and homozygote (-/-)  
723 with the  $\Delta 194$  deletion. The concentrations of plasma TC (b), HDL(c), non-HDL(d)  
724 and TG(e) were measured in WT, vehicle, TMPZ and clodipogrel groups at the  
725 endpoint of this experiment. Differences were assessed by unpaired student t's test or  
726 Mann-Whitney test. \*  $p < 0.05$  versus Vehicle, \*\* $p < 0.01$  versus Vehicle. ## $p < 0.01$   
727 versus WT. All data was expressed as mean  $\pm$  standard error (SEM)

728 **Figure 5.** Histological analysis. (a) Representative images of en face analysis. (b)  
729 Quantitative analysis of lesion areas in whole aortas. Differences were assessed by  
730 unpaired student t's test. (c) Representative images of ORO staining of aortic root  
731 sections. (d) Quantitative analysis of lesion areas in aortic root sections. (e)  
732 Representative images of macrophage (CD68) analysis (b) Quantitative analysis of  
733 lesions area in macrophage analysis. (f) Representative images of SMC (SMA)  
734 analysis (g) Quantitative analysis of lesions area in SMC. Differences were assessed  
735 by unpaired student t's test. \*  $p < 0.05$  versus Vehicle, \*\* $p < 0.01$  versus Vehicle.  
736 # $p < 0.05$  versus clopidogrel. Scale bar=250 $\mu$ m. All data was expressed as mean  $\pm$   
737 SEM.

738 **Figure 6.** Signaling transduction in ADP-mediated platelet activation. (a) Intracellular  
739 calcium concentration. (b) Intracellular cAMP concentration. Western blot analyses of

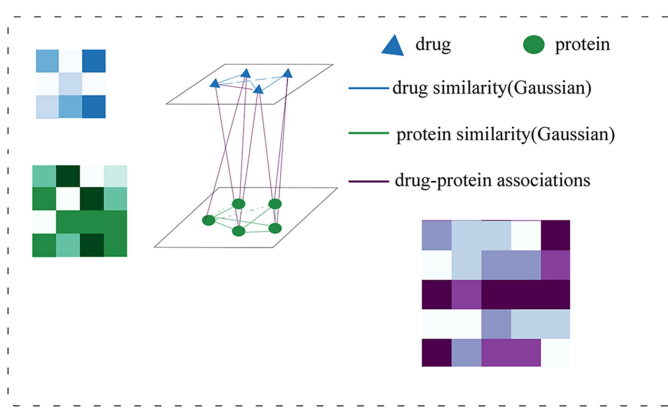
740 the expression of PI3K (c), Akt (d) and p-Akt (d). Differences were assessed by  
741 unpaired student t's test with or without Welch's corrections. \*\*  $p < 0.01$  versus  
742 Vehicle, \*  $p < 0.05$  versus Vehicle. All data was expressed as mean  $\pm$ SEM.

743 **Table**

744 **Table 1** KEGG pathway enrichment analysis of DLDTI results

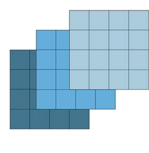
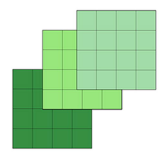
Class	KEGG term	Count	P value
Signal transduction	PI3K-Akt signaling pathway	36	2.49E-17
	Neuroactive ligand-receptor interaction	32	6.04E-17
	MAPK signaling pathway	29	1.08E-13
	Calcium signaling pathway	26	1.01E-15
	Rap1 signaling pathway	22	2.99E-11
	cGMP-PKG signaling pathway	20	2.99E-11
	cAMP signaling pathway	16	3.83E-07
Metabolism	Metabolism of xenobiotics by cytochrome P450	23	4.27E-20
	Steroid hormone biosynthesis	17	1.28E-14
	Retinol metabolism	15	5.89E-12
Immune system	Complement and coagulation cascades	21	3.06E-17
	Th17 cell differentiation	15	1.77E-09
Others	Regulation of actin cytoskeleton	16	6.90E-07
	Gap junction	15	2.74E-10
	Fluid shear stress and atherosclerosis	15	2.91E-08

745

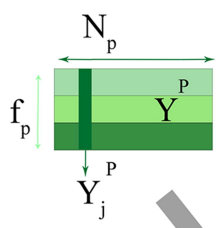


$N_d$ : number of drugs  
 $N_p$ : number of proteins  
 $f_d$ : dimension of drug features  
 $f_p$ : dimension of protein features

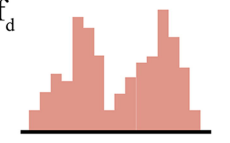
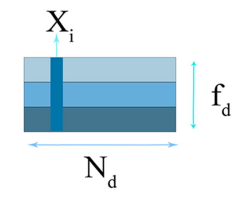
Embedding



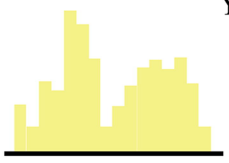
Embedding



Matrix representation of drug (left) and protein(right) features

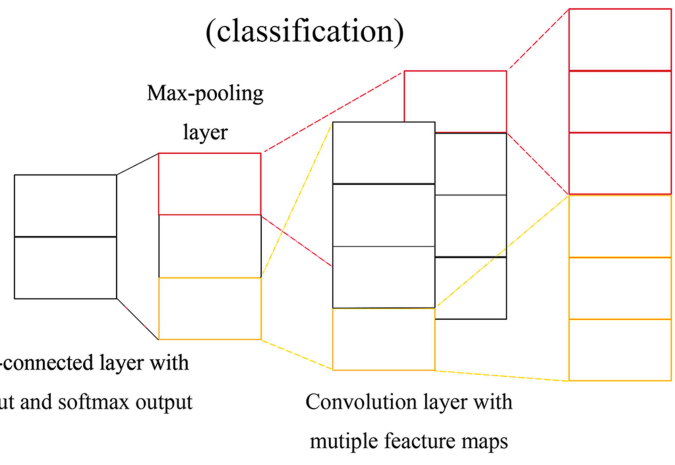


Low dimensional vector representation for each drug vertex

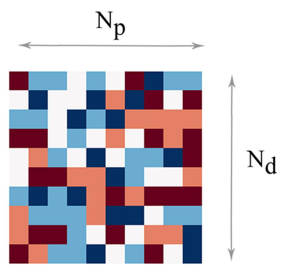


Low dimensional vector representation for each target (protein) vertex

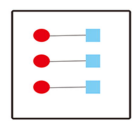
CNN (classification)



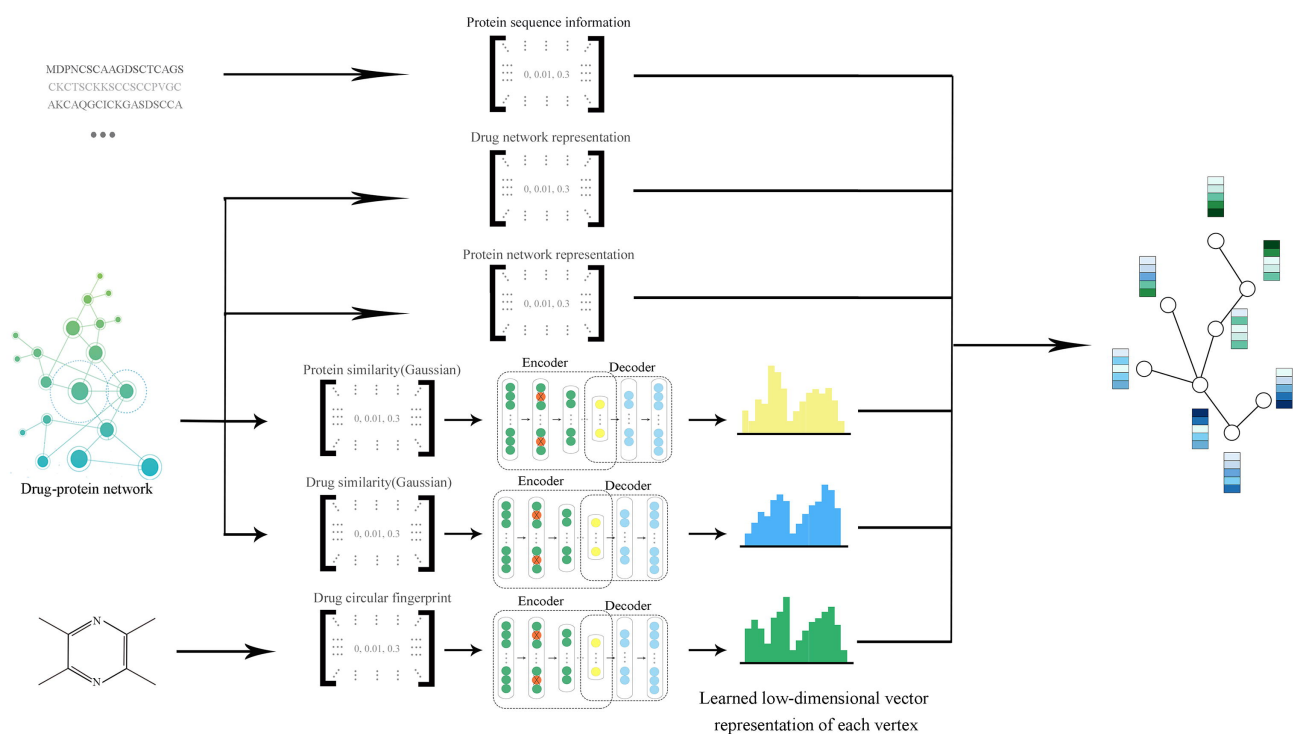
Input vector

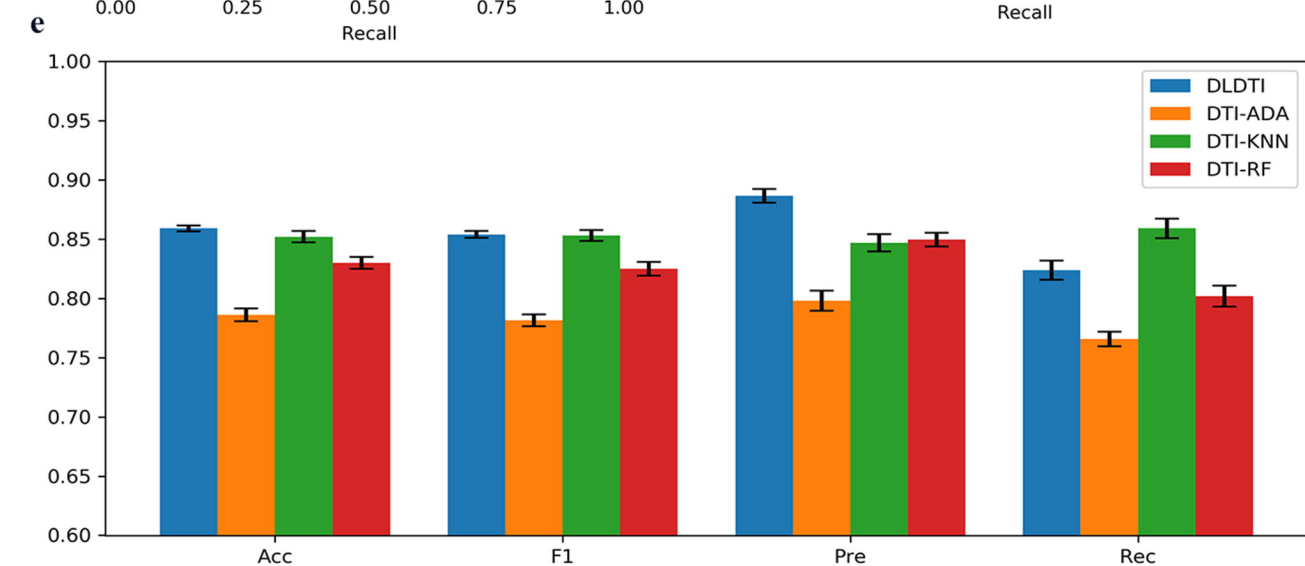
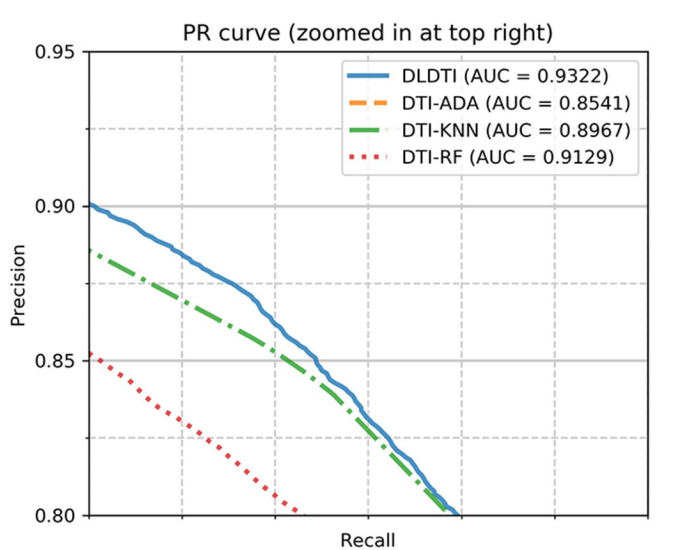
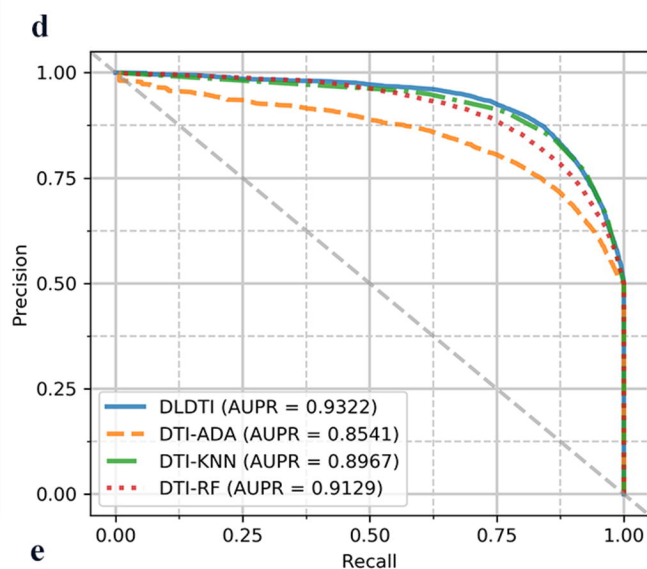
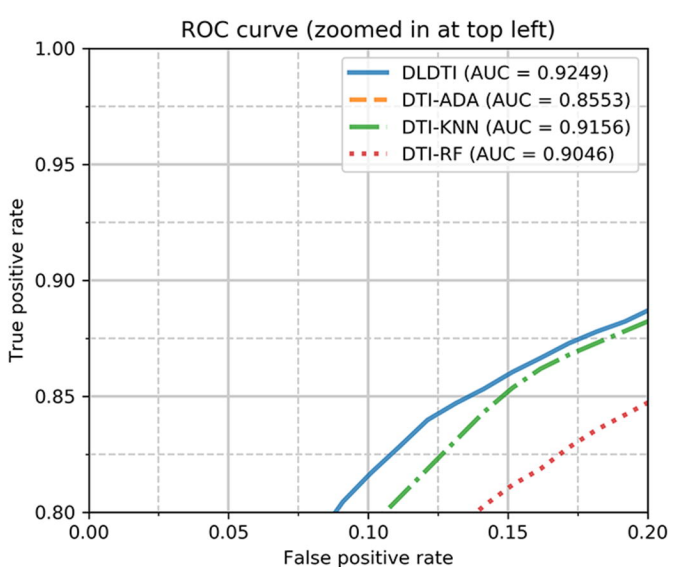
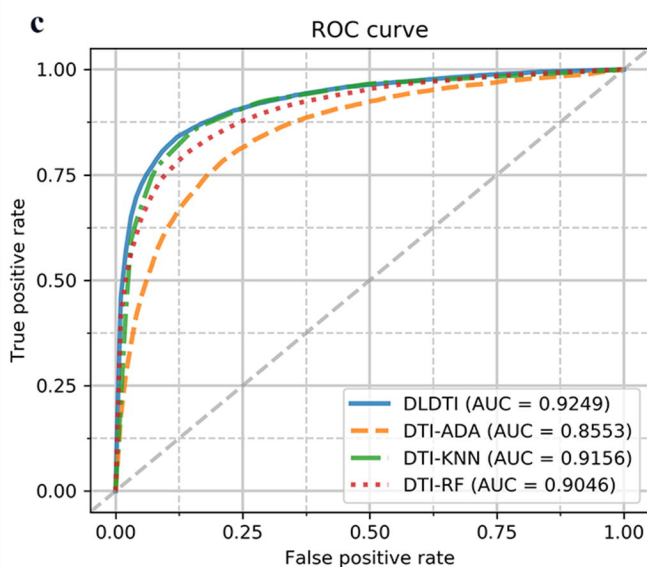
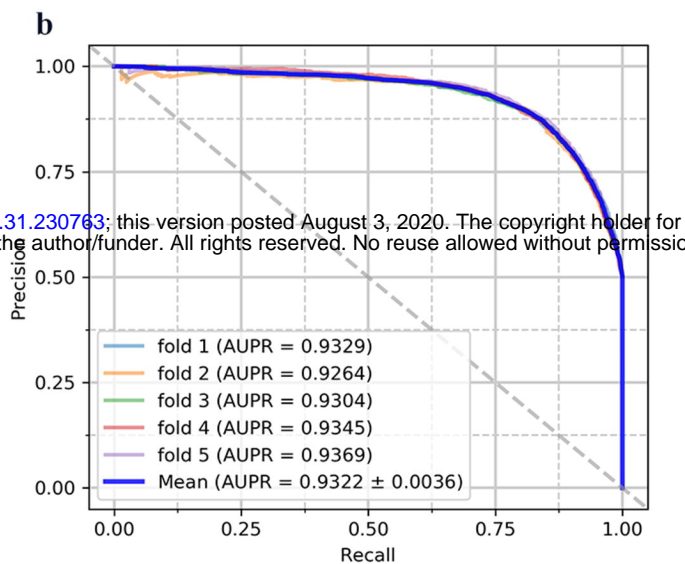
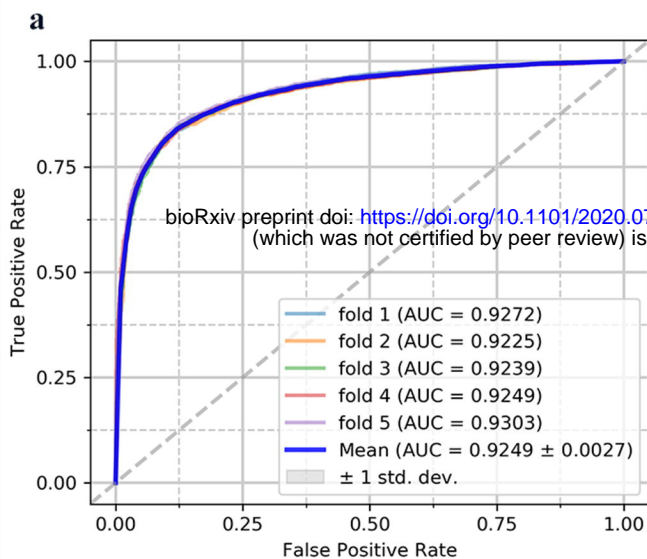


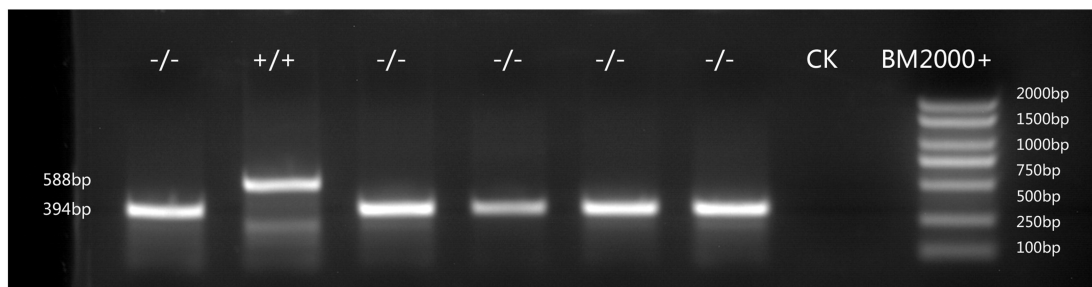
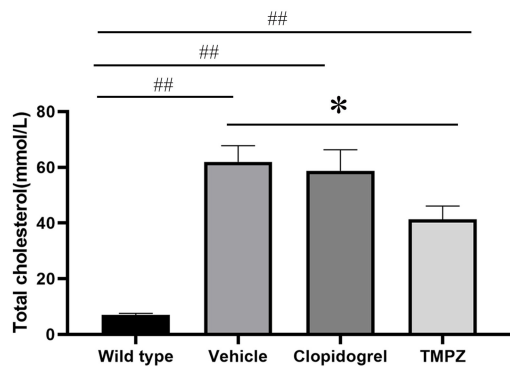
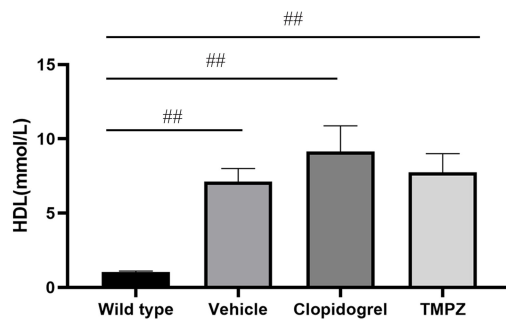
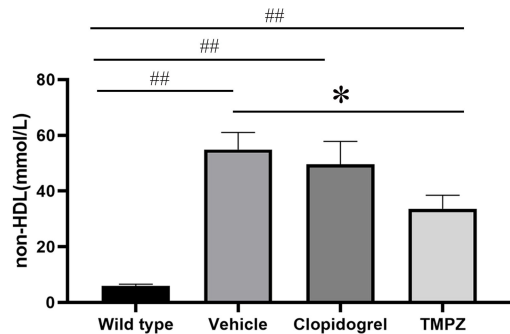
Prediction scores of drug-protein interactions



Analysis and validation





**a****b****c****d****e**